

Frequency-Adaptive Filtering of Low-Frequency Harmonic Current in Fuel Cell Power Conditioning Systems

L. Cao, K. H. Loo, Y. M. Lai *

Abstract

Based on one of the most researched multi-input dc-dc converter topologies for renewable energy systems, the multi-input dual-active bridge (DAB) dc-dc converter, the effectiveness of harmonic current absorption by the energy storage branch in fuel cell power conditioning systems is critically evaluated. The closed-loop output impedances of the converter under single-voltage-loop and dual-loop controls are derived and compared. It is shown that both control strategies can effectively reduce the converter's closed-loop output impedance, thus favoring the flow of harmonic current and prevent it from being drawn from either the fuel cell branch or the dc-link capacitor. However, as shown by experimental results, the use of conventional PI control alone still produces noticeable voltage ripple on the dc voltage bus due to harmonic current being drawn from the dc-link capacitor. Proportional-resonant (PR) control is proposed to effectively compensate for the dc bus voltage variation by generating an extremely low-impedance path for harmonic current flow at specific frequency. An analogue-based frequency tracking circuit is further proposed to adjust the resonant frequency for compensating the effect of harmonic frequency variation.

1 Introduction

Fuel cells have been widely used in clean power generators for converting chemical energy carried by hydrogen-rich fuels to electrical energy. Among the various types of fuel cells, proton-exchange membrane (PEM) fuel cells are currently, and will remain, dominant in medium-power applications such as fuel cell vehicles and stand-alone power generators. However, previous researches on PEM fuel cells show that their lifetime performance and reliability can be adversely affected when they have to handle low-frequency current ripple below 400 Hz [1], [2]. According to [2], fuel cells exhibit hysteresis at low frequencies around 100 Hz

*The authors are with The Department of Electronic and Information Engineering, The Hong Kong Polytechnic University, Hong Kong
Tel: (852) 2766 4744 Fax: (852) 2362 8439 Email: lingling.cao@connect.polyu.hk.

due to the proximity of these frequencies to the natural frequency of the chemical reaction kinetics at the fuel cell electrodes, with time constant governed by the activation loss resistance and double layer capacitor. This hysteretic behavior can cause additional loss to the operation of fuel cells [3]. Another research conducted by Choi *et al* [4] shows that there is a 6% reduction in the available output power when significant low-frequency current ripple is imposed on fuel cells. Recently, Sergi *et al* [5] reported that degradation in the cathode catalyst was observed when fuel cells are subjected to low-frequency current ripple. Although the findings from the current researches do not give a conclusive explanation to the physical relationship between low-frequency current ripple and the lifetime of fuel cells, it is evident that the electrochemistry and thermal properties of PEM fuel cells, and hence, their physical health, are sensitive to low-frequency current ripple.

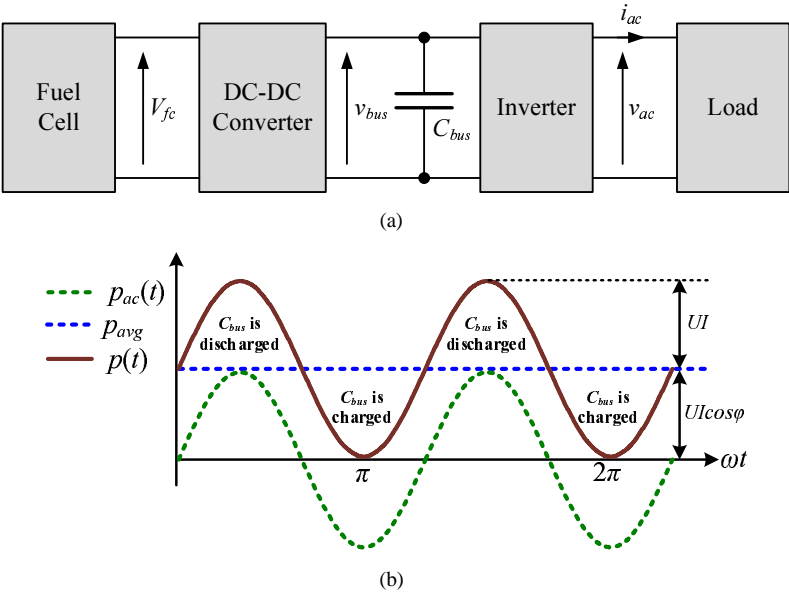


Figure 1: Typical fuel cell power conditioning system: (a) system block diagram, and (b) power demand when a single-phase inverter is connected as load.

In general, for fuel cell power conditioning systems connected to single-phase inverter load, such as that represented in Fig. 1(a), the fuel cell's output current ripple occurs at twice the inverter frequency, typically 100 Hz or 120 Hz. Assuming that the system has an efficiency of 100%, the inverter output voltage and current, and hence, the instantaneous power drawn from the fuel cell, are given by

$$\begin{aligned}
v_{ac}(t) &= \sqrt{2}U \cos \omega t \\
i_{ac}(t) &= \sqrt{2}I \cos (\omega t - \varphi) \\
p(t) &= v_{ac}(t)i_{ac}(t) = UI \cos \varphi + UI \cos (2\omega t - \varphi) = p_{avg} + p_{ac}(t)
\end{aligned} \tag{1}$$

It can be seen that the instantaneous power drawn from the fuel cell is a summation of the dc component p_{avg} and the harmonic component $p_{ac}(t)$ oscillating at twice the inverter frequency. In order to prevent the fuel cell from experiencing excessive power fluctuations, which will degrade its lifetime, the dc-dc converter is typically designed with a very small closed-loop bandwidth so that the fuel cell will mainly deliver the dc power component p_{avg} while the harmonic power component $p_{ac}(t)$ is drawn from the dc-link capacitor C_{bus} . The dc-link capacitor is discharged when $p(t) > p_{avg}$ and is charged when $p(t) < p_{avg}$. These periodic charging and discharging processes will cause the existence of voltage ripple (at twice the inverter frequency) on the dc bus voltage, and the inverter's operation can be adversely affected when the amplitude of the voltage ripple becomes excessively large.

The use of dc-link capacitors for passive filtering of low-frequency harmonic current and preventing them from propagating to fuel cells is traditionally employed in fuel cell power conditioning systems. However, since the dc-link capacitors are required to create an extremely low impedance to the flow of low-frequency harmonic current, the required capacitance is very large (usually mF). Alternatively, a series-connected LC network can be inserted to the capacitor branch to create a zero-impedance branch for bypassing the low-frequency harmonic current when the resonant frequency of the LC network is accurately tuned to the harmonic frequency [6]. However, with this solution, the required inductance is typically very large and such an approach is not applicable to the situation where multiple harmonic currents exist. Instead of reducing the impedance of the capacitor branch, some researchers proposed to increase the impedance of the fuel cell branch [7]–[11]. These methods include using dual-loop control with a very small bandwidth to give a ripple-free reference for the fuel cell current [7], feedforwarding and subtracting the low-frequency ripple derived from the dc bus voltage to generate a ripple-free reference for the fuel cell current [8]–[10], and minimizing the low-frequency ripple on the fuel cell current by proportional-resonant control [11]. Typically, since the harmonic current must be completely delivered by the dc-link capacitor, the capacitance required to maintain a smooth dc bus voltage must remain to be very large. In fact, all the passive-filter-based methods discussed above share a common drawback that large inductors or capacitors are needed for low-frequency harmonic absorption. In contrast, when small dc-link capacitor is used, and large voltage ripple exists on the dc bus voltage, additional control

must be introduced into the inverter for minimizing its effects on the inverter's output voltage [11].

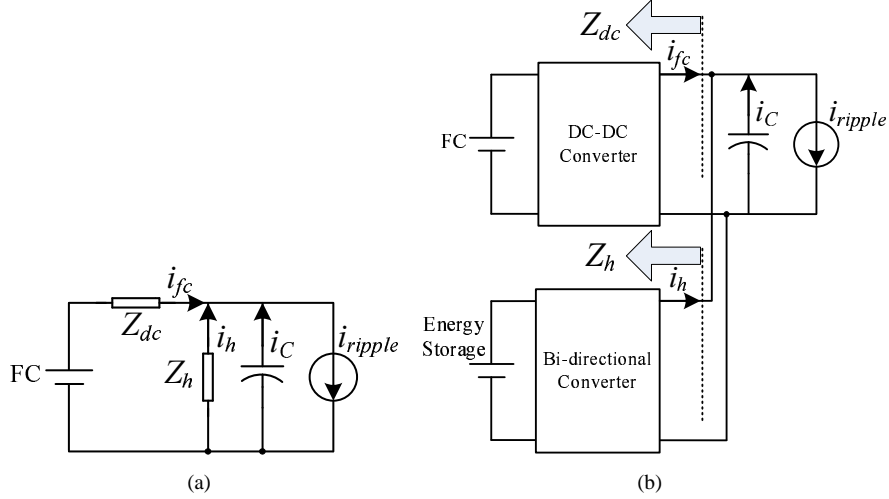


Figure 2: Fuel cell power conditioning system with energy storage: (a) impedance model, and (b) practical implementation of system.

To overcome this limitation, active-filter-based methods should be employed, where energy storages such as batteries and supercapacitors are interfaced to the dc voltage bus through the use of bi-directional dc-dc converters [12]–[14]. Since the dc-dc converters are typically configured to tightly regulate the dc bus voltage, thus behaving as voltage source, they are effectively characterized by low output impedance that favors harmonic current flow. Fig. 2(a) shows the harmonic current i_h contributed by the bi-directional converter having an effective output impedance of Z_h in addition to those contributed by the fuel cell (i_{fc}) and dc-link capacitor (i_C). To minimize the harmonic current drawn from the fuel cell, it is required that either the impedance of the fuel cell branch Z_{dc} is increased or the impedance of the bi-directional dc-dc converter Z_h is reduced by means of suitable controller designs.

Due to the slow dynamic response of the fuel cell branch, which suffers from the time lags associated with the fuel supply system and fuel cell's internal electrochemical processes, the use of active filter with energy storage and bi-directional dc-dc converter is beneficial in terms of improving the overall dynamic response of the fuel cell-energy storage system. Such a system configuration is therefore capable of meeting the double requirements of effective harmonic current absorption by the converter-interfaced energy storage and tight regulation of the dc bus voltage by fast voltage control. Various control strategies have been proposed for achieving the desired control objectives. The most common one is to control the system in such a way that the fuel cell branch delivers the average load power while the energy storage branch compensates for any power surplus or deficit due to transient load power variations [15], [16]. An alternative approach is to employ one outer voltage

loop that generates the current references for the inner current loops of the fuel cell and energy storage branches, which makes them share the total transient load power demand [17]. Lastly, in [18], the energy storage branch is controlled as current source while the fuel cell branch is responsible for dc bus voltage regulation.

In general, the control strategies for parallel-connected fuel cell-energy storage systems can be broadly classified into three categories as depicted in Fig. 3: (a) fuel cell branch controlled as current source and energy storage branch controlled as voltage source, (b) fuel cell branch controlled as voltage source and energy storage branch controlled as current source, and (c) both fuel cell and energy storage branches controlled as current sources. In general, fuel cells are characterized by slow dynamic response and lifetime degradation if they are subjected to frequent power fluctuations. These characteristics render the fuel cell branch unsuitable for dc bus voltage regulation, hence control strategy (b) should be avoided. Control strategy (c) is feasible with the fuel cell branch configured to respond to slow power changes while the energy storage branch responds to fast power changes, and dc bus voltage regulation is achieved when the combined slow and fast power changes of the two branches equal the load power changes. The drawback of this control strategy is, however, that the energy storage branch will not compensate for the slow power changes even if the fuel cell branch fails to meet them due to various reasons, such as fuel starvation, which can lead to stability problems of the hybrid system. In comparison to the previous two strategies, control strategy (a) offers more versatility in applications. Since the energy storage branch is configured to regulate the dc bus voltage, it will respond to all power changes that cannot be met by the fuel cell branch. Hence, the fuel cell branch can be configured to operate in load-following mode or constant-power mode depending on applications. Any power surplus or deficit caused by the fuel cell branch will be compensated by the energy storage branch. Under this control strategy, the energy storage branch therefore plays a critical role in both aspects of achieving a tight dc bus voltage regulation and absorption of harmonic current.

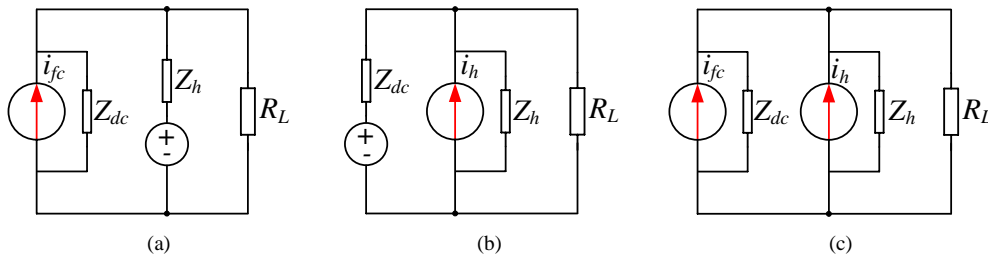


Figure 3: Possible control strategies in fuel cell-energy storage system: (a) fuel cell branch controlled as current source and energy storage branch controlled as voltage source, (b) fuel cell branch controlled as voltage source and energy storage branch controlled as current source, and (c) both fuel cell and energy storage branches controlled as current sources.

As the energy storage branch, typically made up of battery or supercapacitor banks, is known to exhibit

fast dynamic characteristic, the overall performance of fuel cell-energy storage systems, as discussed above, then relies heavily on the performance of the bi-directional dc-dc converter interface. In this paper, the effects of various control strategies are discussed from an output-impedance viewpoint. A bi-directional dual active bridge (DAB) dc-dc converter modified for multi-input operation is chosen as the platform for analysis due to its common use in renewable energy systems employing multiple dc energy sources. Proportional-resonant (PR) control, which is commonly used in grid-connected inverters for harmonic suppression, is proposed to be used here for the attenuation of the 100/120-Hz harmonic current by implementing it on the bi-directional converter. To account for the possible variations of the inverter frequency, such as that occurs when grid-connected inverters operate in the presence of grid frequency variations [19] or when paralleled inverters are controlled by droop method in a standalone microgrid [20], a frequency-adaptive PR controller is proposed to ensure an effective harmonic current absorption under variable inverter frequency.

This paper is organized as follows. In Section 2, the operating principle of the multi-input bi-directional DAB dc-dc converter is discussed and the main small-signal transfer functions are given. In Section 3, these transfer functions are used to derive the converter's closed-loop output impedances under various voltage-control strategies. For extending the effectiveness of voltage-control strategies on suppressing the harmonic current being drawn from the fuel cell branch, a frequency-adaptive PR controller capable of tracking the harmonic frequency of interest is proposed for further reducing the closed-loop output impedance of the energy storage branch at the frequency being tracked, and its design and implementation are discussed in Section 4. An experimental prototype of the PR-controlled two-input bi-directional DAB dc-dc converter is constructed and experimental results are discussed in Section 5. Finally, conclusion is given in Section 6.

2 Multi-Input Bi-Directional Dual Active Bridge DC-DC Converter

2.1 Steady-State Operation

Bi-directional dual active bridge (DAB) dc-dc converters are widely used in renewable-energy-based power conditioning systems due to several advantages such as flexible power flow control, realization of zero-voltage switching, and high efficiency. In this paper, a phase-shift-controlled current-fed DAB dc-dc converter is selected as the platform for implementing the proposed frequency-adaptive proportional-resonant (PR) control. In comparison to the original topology discussed in [21], the modified converter shown in Fig. 4 uses two separate transformers for the input half-bridge cells (instead of one transformer with three windings) so that each of the input half-bridge cells can be controlled independently, thus enabling a more versatile implementation of

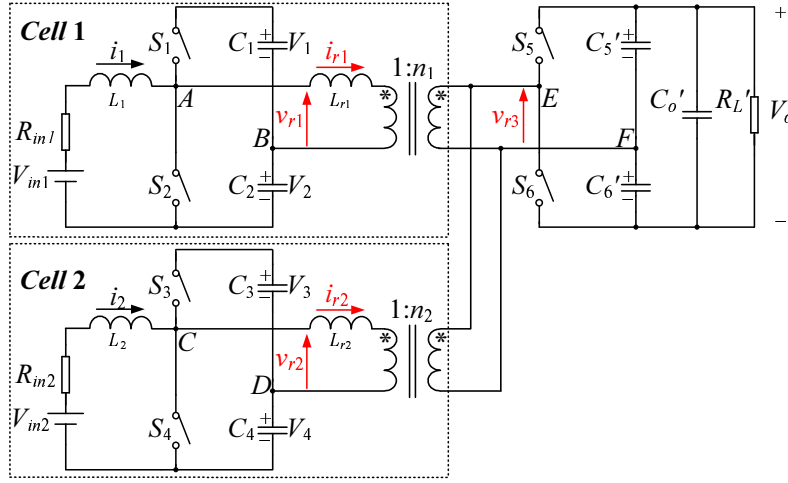


Figure 4: Multi-input bi-directional DAB dc-dc converter with shared secondary half-bridge cell.

various power-flow control strategies. By using phase-shift control, the bi-directional power flow of each of the input half-bridge cells can be controlled by adjusting the phase difference between the transformer's primary and secondary voltages.

Referring to Fig. 4, $v_{r1} \sim v_{r2}$, and v_{r3} represents the output voltages of the two input half-bridge cells and the shared secondary half-bridge cell, respectively. The capacitors $C_1 \sim C_4$ and $C'_5 \sim C'_6$ are assumed to be sufficiently large that the voltages $V_1 \sim V_4$ and $V'_5 \sim V'_6$ are reasonably assumed to be constant. The current flowing through the transformer's leakage inductance of input half-bridge cell 1 and 2 is denoted by i_{r1} and i_{r2} , respectively. By controlling the power flows of both input half-bridge cells, three operating modes are realizable on the converter: (1) both input half-bridge cells deliver power to the load; (2) one input half-bridge cell delivers power to the load while the other absorbs power; and (3) one input half-bridge cell delivers power to the load while the other is at rest. The main operating waveforms of the converter for case (1) and (2) are illustrated in Fig. 5.

It can be seen from Fig. 5 that the input half-bridge cell delivers power when $\varphi > 0$ and absorbs power when $\varphi < 0$, where φ is the phase difference between the transformer's primary and secondary voltages. For the two-input converter shown in Fig. 4, the power delivered by input half-bridge cell 1 and 2, and the total power delivered by both, is given by Equation (2), (3), and (4), respectively.

$$P_1 = \frac{\int_0^{2\pi} i_{r1}(\theta)v_{r1}(\theta) d\theta}{2\pi} = \frac{\varphi_1 (\pi - |\varphi_1|)}{4\pi L_{r1}\omega} \frac{V_{12}V'_{56}}{n_1} \quad (2)$$

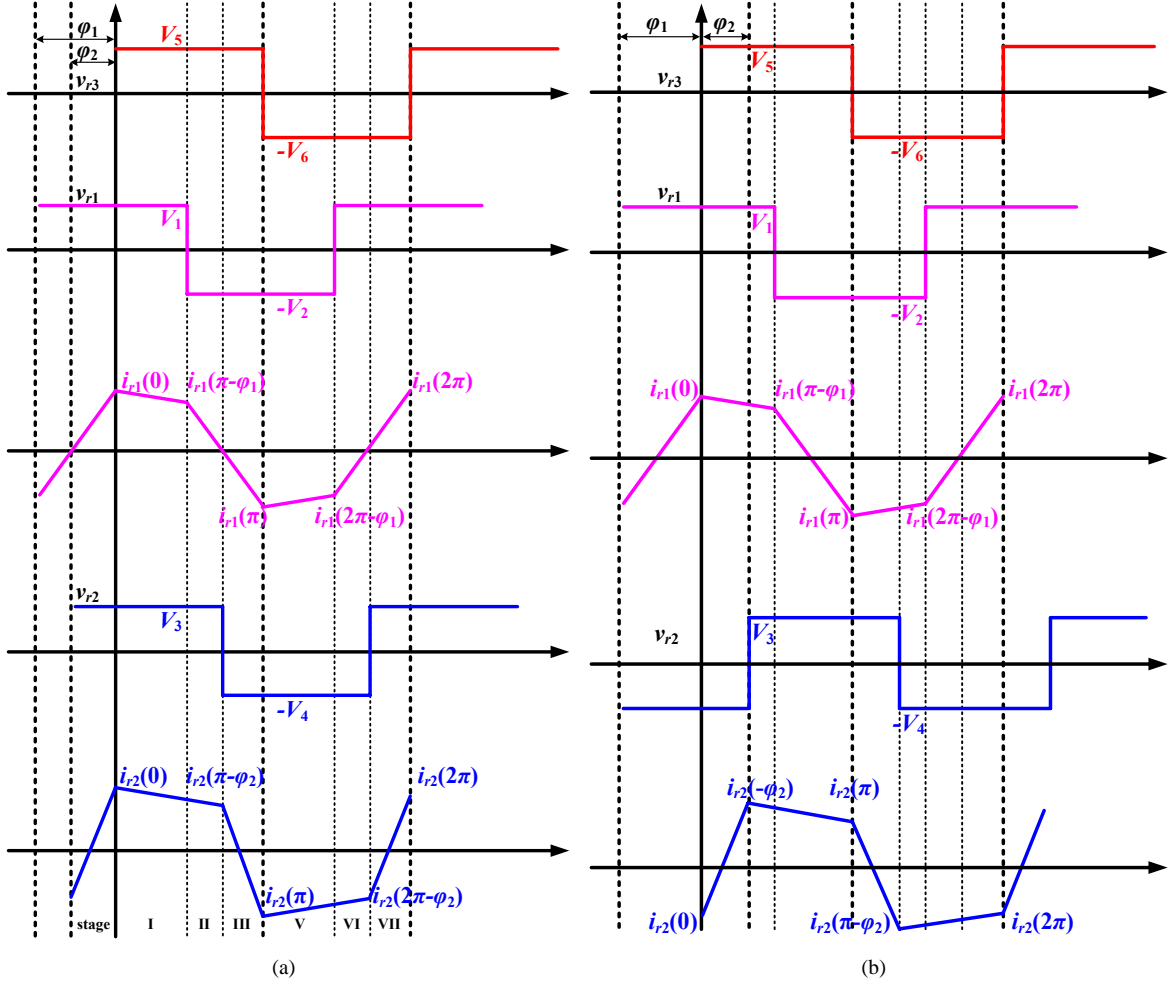


Figure 5: Main converter's operating waveforms (a) when both input half-bridge cells deliver power to the load, and (b) when one input half-bridge cell delivers power to the load while the other absorbs power.

$$P_2 = \frac{\int_0^{2\pi} i_{r2}(\theta)v_{r2}(\theta) d\theta}{2\pi} = \frac{\varphi_2(\pi - |\varphi_2|)}{4\pi L_r 2\omega} \frac{V_{34} V'_{56}}{n_2} \quad (3)$$

$$P_o = P_1 + P_2 \quad (4)$$

where $V_{12} = (V_1 + V_2)$, $V_{34} = (V_3 + V_4)$, and $V'_{56} = (V'_5 + V'_6) = V_o$.

2.2 Small-Signal Transfer Functions

Since the two-input bi-directional DAB dc-dc converter shown in Fig. 4 is effectively two single-input converters connected in parallel, each of them will exhibit the same small-signal characteristics. Hence, the

small-signal transfer functions required for output impedance analysis can be obtained by considering a single-input converter. The state vector \tilde{x} and input vector \tilde{u} are defined as follows.

$$\tilde{x} = \begin{bmatrix} \tilde{i}_L & v_{\tilde{1}2} & v_{\tilde{5}6} \end{bmatrix}^T \quad (5)$$

$$\tilde{u} = \begin{bmatrix} v_{\tilde{i}n} & \tilde{\varphi} & \tilde{i}_o \end{bmatrix}^T \quad (6)$$

where, in Equation (5), \tilde{i}_L is the boost inductor current, $v_{\tilde{1}2}$ (or $v_{\tilde{3}4}$) is the total voltage across the input capacitors ($\tilde{v}_1 + \tilde{v}_2$) (or $(\tilde{v}_3 + \tilde{v}_4)$), $v_{\tilde{5}6}$ is the total output voltage across the output capacitors ($\tilde{v}'_5 + \tilde{v}'_6$) reflected to the transformer's primary, and, in Equation (6), $v_{\tilde{i}n}$ is the converter's input voltage, $\tilde{\varphi}$ is the phase difference between the transformer's primary and secondary voltages, and \tilde{i}_o is the converter's output (load) current.

With the input and state vectors defined, the converter's small-signal state-space model can be conveniently represented in the following standard form.

$$\dot{\tilde{x}} = A\tilde{x} + B\tilde{u} \quad (7)$$

where

$$A = \begin{bmatrix} 0 & -\frac{1}{2L} & 0 \\ \frac{1}{C_p} & 0 & \frac{-\varphi(\pi-|\varphi|)}{2\pi L_r \omega C_p} \\ 0 & \frac{\varphi(\pi-|\varphi|)}{2\pi L_r \omega (2C_o + C_s)} & \frac{-2}{R_L(2C_o + C_s)} \end{bmatrix} \quad (8)$$

$$B = \begin{bmatrix} \frac{1}{L} & 0 & 0 \\ 0 & \frac{-V_{56}(\pi-2|\varphi|)}{2\pi L_r \omega C_p} & 0 \\ 0 & \frac{V_{34}(\pi-2|\varphi|)}{2\pi L_r \omega (2C_o + C_s)} & \frac{-2}{R_L(2C_o + C_s)} \end{bmatrix} \quad (9)$$

In Equations (8) and (9), L is the inductance of the boost inductor (L_1 or L_2), L_r is the leakage inductance (L_{r1} or L_{r2}), C_p is the input capacitor ($C_1 \sim C_4$), and, C_s , C_o , and R_L denotes the dc-link capacitor for secondary half-bridge (C'_5 or C'_6), the output dc-link capacitor (C'_o), and the load resistor (R'_L) reflected to the transformer's primary, respectively. The transfer functions from the inputs ($v_{\tilde{i}n}$, $\tilde{\varphi}$, \tilde{i}_o) to the boost inductor current \tilde{i}_L and converter's output voltage \tilde{v}_o can be obtained by solving Equations (10) and (11). The results are summarized in Table 2.

$$\tilde{i}_L = \begin{bmatrix} 1 & 0 & 0 \end{bmatrix} (sI - A)^{-1} B\tilde{u} = G_{ig}\tilde{v}_{in} + G_{i\varphi}\tilde{\varphi} + G_{ii}\tilde{i}_o \quad (10)$$

$$\tilde{v}_o = \begin{bmatrix} 0 & 0 & 1 \end{bmatrix} (sI - A)^{-1} B\tilde{u} = G_{vg}\tilde{v}_{in} + G_{v\varphi}\tilde{\varphi} - Z_o\tilde{i}_o \quad (11)$$

Table 1: Definitions of small-signal transfer functions of a single-input bi-directional DAB dc-dc converter.

Symbol	Definition
$G_{ig}(s)$	Input-voltage-to-inductor-current transfer function
$G_{i\varphi}(s)$	Phase-shift-angle-to-inductor-current transfer function
$G_{ii}(s)$	Load-current-to-inductor-current transfer function
$G_{vg}(s)$	Input-voltage-to-output-voltage transfer function
$G_{v\varphi}(s)$	Phase-shift-angle-to-output-voltage transfer function
$Z_o(s)$	Load-current-to-output-voltage transfer function (or output impedance)

3 Output Impedance Analysis

It has been discussed previously that the fuel cell branch is considered unsuitable for dc bus voltage regulation due to its slow dynamic response, hence it is typically configured to deliver the average load power while the energy storage branch achieves dc bus voltage regulation by compensating for any transient power surplus or deficit. This control strategy, where the fuel cell branch is controlled as current source and the energy storage branch is controlled as voltage source, is adopted in this paper, and the equivalent circuit is shown in Fig. 3(a). In general, two voltage-control strategies can be implemented on the energy storage branch by employing: (1) single voltage loop, and (2) dual (outer voltage and inner current) loop. The main control objective of the energy storage branch is to tightly regulate the dc bus voltage v_o . The two voltage-control strategies applicable to the energy storage branch are represented by the block diagrams shown in Fig. 6.

Since the harmonic current drawn by the inverter load will mainly flow from the energy storage branch, the

Table 2: Small-signal transfer functions of a single-input bi-directional DAB dc-dc converter.

$G_{ig}(s)$	$\frac{1}{L} \cdot \frac{s^2 + \left[\frac{2}{(2C_o + C_s)RL} \right] s + \frac{\varphi^2(\pi - \varphi)^2}{4\pi^2 C_p(2C_o + C_s)L_r^2 \omega^2}}{s^3 + \left[\frac{2}{(2C_o + C_s)RL} \right] s^2 + \left[\frac{1}{2C_p L_{dc}} + \frac{\varphi^2(\pi - \varphi)^2}{4\pi^2 C_p(2C_o + C_s)L_r^2 \omega^2} \right] s + \frac{1}{C_p(2C_o + C_s)LR_L}}$
$G_{i\varphi}(s)$	$\frac{V_{in}(\pi - 2 \varphi)}{2\pi C_p LL_r \omega} \cdot \frac{s + \frac{\varphi(\pi - \varphi)}{2\pi(2C_o + C_s)L_r \omega} + \frac{2}{(2C_o + C_s)RL}}{s^3 + \left[\frac{2}{(2C_o + C_s)RL} \right] s^2 + \left[\frac{1}{2C_p L} + \frac{\varphi^2(\pi - \varphi)^2}{4\pi^2 C_p(2C_o + C_s)L_r^2 \omega^2} \right] s + \frac{1}{C_p(2C_o + C_s)LR_L}}$
$G_{ii}(s)$	$\frac{-\varphi(\pi - \varphi)}{2\pi C_p(2C_o + C_s)LL_r \omega} \cdot \frac{1}{s^3 + \left[\frac{2}{(2C_o + C_s)RL} \right] s^2 + \left[\frac{1}{2C_p L} + \frac{\varphi^2(\pi - \varphi)^2}{4\pi^2 C_p(2C_o + C_s)L_r^2 \omega^2} \right] s + \frac{1}{C_p(2C_o + C_s)LR_L}}$
$G_{vg}(s)$	$\frac{RL\varphi(\pi - \varphi)}{4\pi C_p LL_r \omega} \cdot \frac{1}{\left[\frac{(2C_o + C_s)RL}{2} \right] s^3 + s^2 + \left[\frac{(2C_o + C_s)RL}{4C_p L} + \frac{RL\varphi^2(\pi - \varphi)^2}{8\pi^2 C_p L_r^2 \omega^2} \right] s + \frac{1}{2C_p L}}$
$G_{v\varphi}(s)$	$\frac{RLV_{in}(\pi - 2 \varphi)}{2\pi L_r \omega} \cdot \frac{s^2 - \frac{\varphi(\pi - \varphi)}{2\pi C_p L_r \omega} s + \frac{1}{2C_p L}}{\left[\frac{(2C_o + C_s)RL}{2} \right] s^3 + s^2 + RL \left[\frac{2C_o + C_s}{4C_p L} + \frac{\varphi^2(\pi - \varphi)^2}{8\pi^2 C_p L_r^2 \omega^2} \right] s + \frac{1}{2C_p L}}$
$Z_o(s)$	$\frac{s^2 + \frac{1}{2C_p L}}{\left(\frac{2C_o + C_s}{2} \right) s^3 + \left[\frac{1}{2C_p L} + \frac{\varphi^2(\pi - \varphi)^2}{4\pi^2 C_p(2C_o + C_s)L_r^2 \omega^2} \right] s + \left(\frac{2C_o + C_s}{2} \right) s}$

output impedance of the energy storage branch is thus of greater interest and will be analyzed in more detail. For this purpose, the control block diagrams shown in Fig. 6 are converted into the corresponding signal-flow diagrams for easier visualization. The resulting signal-flow diagrams are depicted in Fig. 7.

By using Mason's formula and the converter's small-signal transfer functions tabulated in Table 2, the converter's closed-loop output impedances under single-voltage-loop control, $Z_{o,v}$, and dual-loop control, $Z_{o,v+i}$, can be derived and the results are summarized in Table 3 and plotted in Fig. 8. For both cases, the converter's closed-loop bandwidth was limited to well below the frequencies of the RHP zeros, and, for single-voltage-loop control, the poles on the imaginary axis too. It can be seen that the converter's output impedance at the harmonic frequency of interest, *i.e.* 100 or 120 Hz, has been strongly attenuated compared to the open-loop case. Both control strategies show similar performances at 100 or 120 Hz, although dual-loop control slightly outperforms single-voltage-loop control at low frequencies. In this work, single-voltage-loop control is used, for it has a simpler structure while showing a similar performance as dual-loop control at the harmonic frequency of interest.

Table 3: Closed-loop output impedances under two voltage-control strategies.

Single-voltage-loop control $Z_{o,v}(s)$	$\frac{Z_o(s)}{1 + F_v F_m G_{vc}(s) G_{v\varphi}(s)}$
Dual-loop control $Z_{o,v+i}(s)$	$\frac{[1 + F_i F_m G_{LPF}(s) G_{ic}(s) G_{i\varphi}(s)] Z_o(s) + F_i F_m G_{ii}(s) G_{LPF}(s) G_{ic}(s) G_{v\varphi}(s)}{1 + F_i F_m G_{LPF}(s) G_{ic}(s) G_{i\varphi}(s) + F_v F_m G_{ic}(s) G_{v\varphi}(s) G_{vc}(s)}$

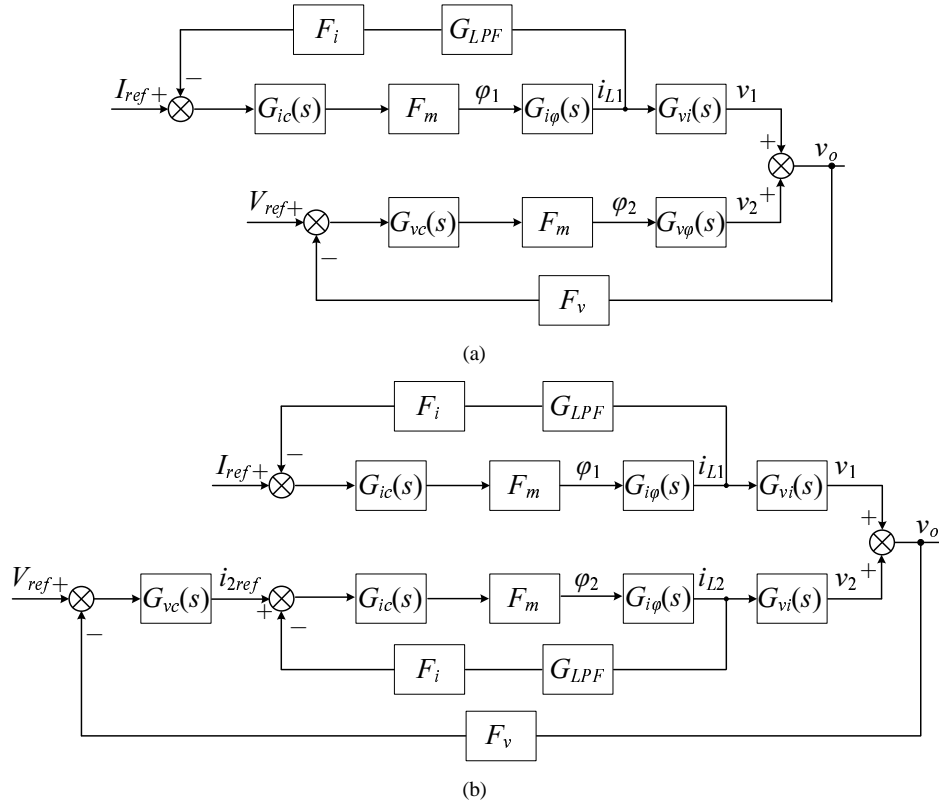


Figure 6: Control strategies for two-input bi-directional DAB dc-dc converter: (a) constant current control (fuel cell branch) and single-voltage-loop control (energy storage branch), (b) constant current control (fuel cell branch) and dual-loop control (energy storage branch).

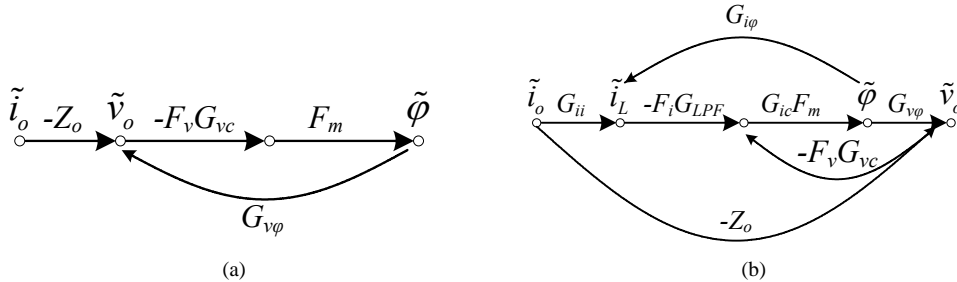


Figure 7: Signal-flow diagram for (a) single-voltage-loop control, and (b) dual-loop control.

4 Frequency-Adaptive Proportional-Resonant Control

It has been shown that the output impedance of the energy storage branch can be effectively reduced by tightly regulating the dc bus voltage using either single-voltage-loop or dual-loop control. As the converter's closed-loop output impedance is related to the magnitude of its loop gain, a further suppression of the harmonic currents being drawn from the fuel cell branch can be achieved by increasing its loop gain at the har-

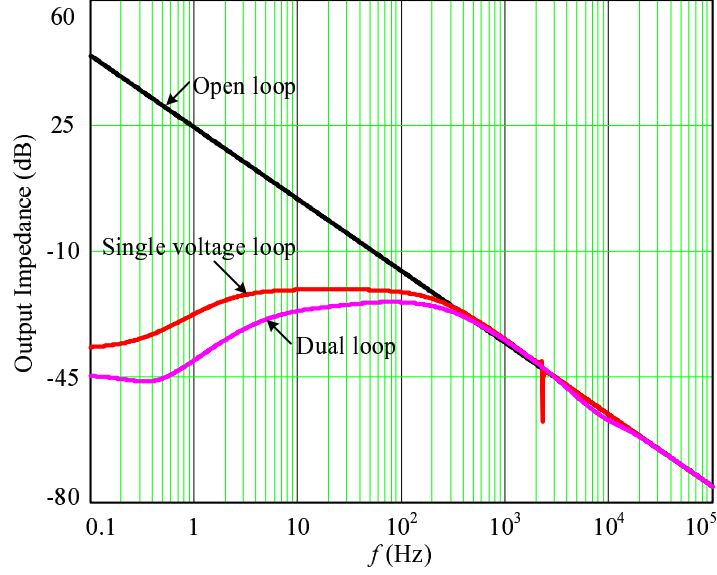


Figure 8: Closed-loop output impedances under two voltage-control strategies.

monic frequencies. Ideally, the harmonic currents will be completely delivered by the converter that offers infinite loop gain at the harmonic frequencies. Proportional-resonant (PR) control, which is frequently used in grid-connected inverter systems [22] and recently in dc-dc converters [23]-[24], is attractive in the way that it provides large amplification of loop gain at selected frequencies only and has a unity gain elsewhere. This allows a PR controller to be conveniently cascaded with the conventional PID controller designed to meet certain steady-state and transient response requirements.

The transfer function of a general PR controller $G_{PR}(s)$ is given by Equation (12), where ω_h is the resonance frequency (or the harmonic frequency to be suppressed), h is the harmonic order, and Q is the quality factor. The bode plots of $G_{PR}(s)$ for various quality factors are shown in Fig. 9. It can be seen that a higher quality factor will introduce more phase lag to the converter's loop gain and the maximum permissible quality factor must be considered when designing the controller for closed-loop stability. By inserting the PR controller with $Q = 5$ and $f_h = \omega_h/2\pi = 100$ Hz into the loop gain designed for single-voltage-loop control, the resulting bode plots and closed-loop output impedances before and after the addition of PR control are shown in Fig. 10 and Fig. 11, respectively.

$$G_{PR}(s) = \left[\sum_{h=2,3,5,7,\dots} \left(\frac{\omega_h s}{s^2 + \omega_h s/Q + \omega_h^2} \right) \right] + 1 \quad (12)$$

To account for the possible variations of inverter frequency [19], [20], it is required that the resonant peak

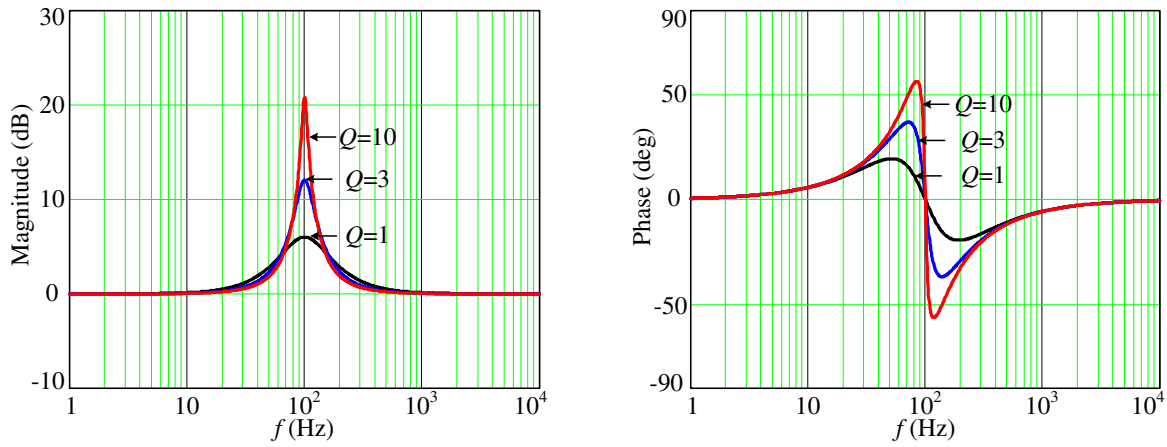


Figure 9: Bode plots of PR controller's transfer function for various quality factors.

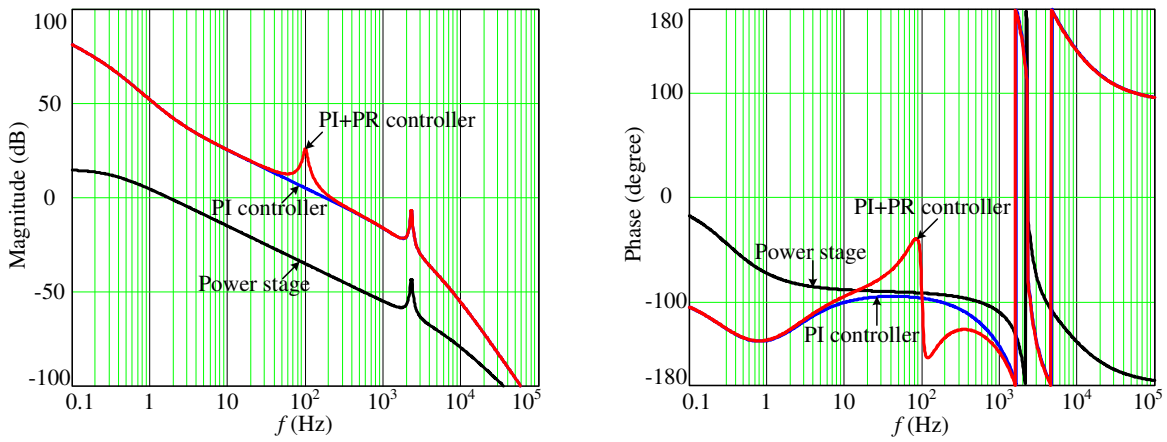


Figure 10: Bode plots of loop gain designed with PI control only and PI+PR control.

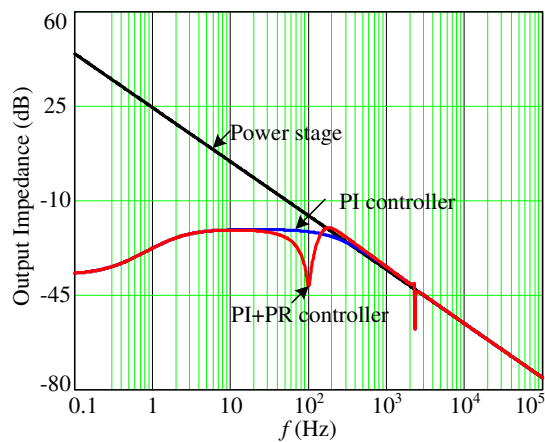


Figure 11: Closed-loop output impedances designed with PI control only and PI+PR control.

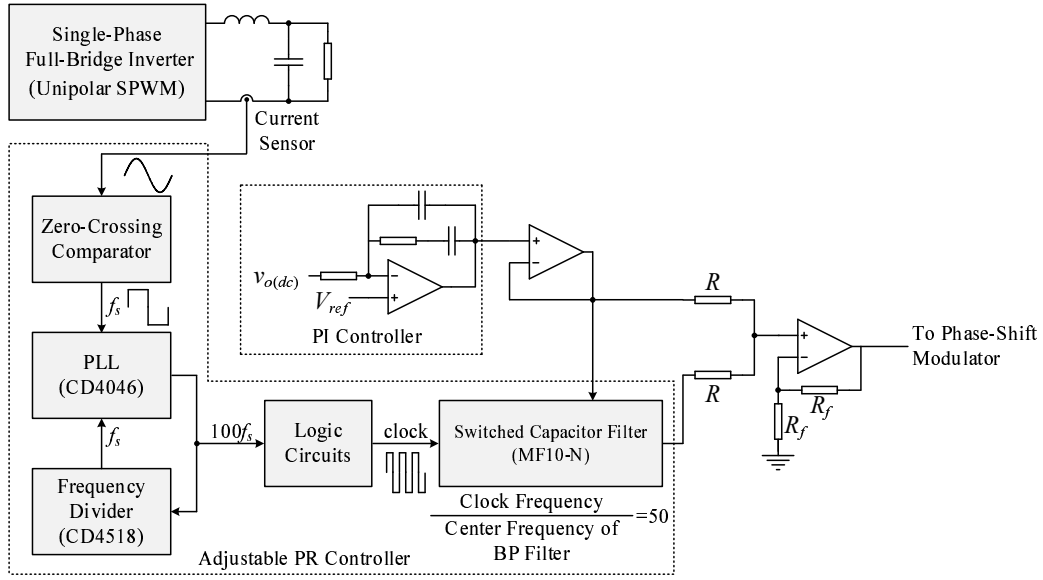


Figure 12: Implementation of frequency-adaptive PR controller.

of the PR controller be synchronized with the inverter frequency in order to generate and maintain a very high loop gain, and hence a very low closed-loop output impedance, of the energy storage branch at the harmonic frequency of interest. For this purpose, a frequency-adaptive PR controller is proposed with the implementation shown in Fig. 12. It operates by sampling the real-time inverter frequency f_s by detecting the zero-crossings of the inverter current waveform. The output of the zero-crossing detector is a bipolar square wave at f_s that forms the reference input to the phase-locked loop (PLL). The PLL tracks the inverter frequency f_s and produces an output signal with frequency in multiples of f_s . Since the center frequency of the switched capacitor bandpass filter (f_o) is defined by dividing its clock frequency by a predefined factor, the PLL's output frequency is set to $100f_s$ and the frequency division factor of the bandpass filter is set to 50 in order to realize $f_o = 2f_s$. Finally, the input of the bandpass filter is added to its output by using a summing amplifier for realizing the '+1' term in Equation (12). It should be noted that the overall effect of inserting the PR controller is to provide a high gain at $2f_s$ only, which is particularly valid when Q is high, while the converter's loop gain outside $2f_s$ remains dominantly shaped by the PI controller.

5 Experimental Verification

A prototype of two-input bi-directional DAB dc-dc converter employing the proposed frequency-adaptive PR control is constructed with the specifications listed in Table 4. In the experiment, the fuel cell unit is

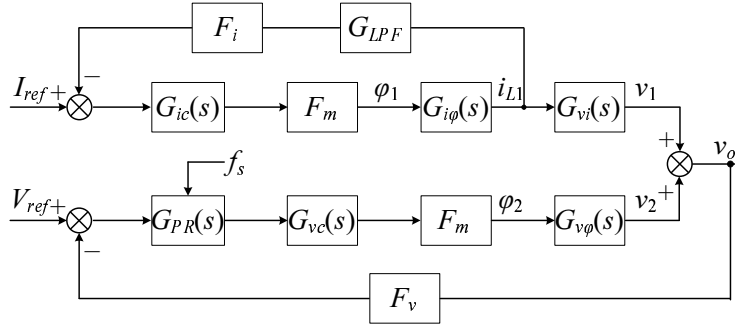


Figure 13: Modified control strategy for two-input bi-directional DAB dc-dc converter (with PR control and grid-frequency tracking) – constant current control (fuel cell branch) and single-voltage-loop control with PR (energy storage branch)

emulated by using a dc power source, and to avoid low-frequency harmonic current being drawn from the fuel cell branch, its closed-loop bandwidth is designed to be 7 Hz, *i.e.* $< 1/10$ of the harmonic frequency at 100 or 120 Hz. Lead-acid batteries are used as energy storage, with four 12-V, 18-Ah batteries connected in series. The closed-loop bandwidth of the battery branch is designed to be approximately 180 Hz to provide non-minimal gain at 100 or 120 Hz while avoiding the effects of the RHP zeros and poles on the imaginary axis. The inverter is a conventional one based on full-bridge topology driven by sinusoidal PWM.

Table 4: Specifications of the two-input bi-directional DAB dc-dc converter prototype.

Description	Parameter	Value
Fuel cell's output power	P_{fc}	160 W
Fuel cell's terminal voltage	V_{fc}	20 V
Transformer's leakage inductance (fuel cell branch)	L_{r1}	4.7 μ H
Transformer's turn ratio (fuel cell branch)	$N_{p1} : N_{s1}$	1:10
Dc-link capacitor for input half-bridge (fuel cell branch)	C_{p1}	80 μ F
Maximum battery power	P_{bat}	160 W
Battery's terminal voltage	V_{bat}	48 V
Transformer's leakage inductance (battery branch)	L_{r2}	25.5 μ H
Transformer's turn ratio (battery branch)	$N_{p2} : N_{s2}$	6:25
Dc-link capacitor for input half-bridge (battery branch)	C_{p2}	6 μ F
Dc-link capacitor for secondary half-bridge	C_s	100 μ F
Output dc bus voltage	V_o	400 V
Output dc-link capacitor	C_o	470 μ F
Switching frequency	f_{sw}	52 kHz

The circuit implementation of the overall dc bus voltage controller of the two-input bi-directional DAB dc-dc converter is shown in Fig. 14. The fuel cell branch is controlled by a simple PI-based constant-current controller that produces a control signal for the UCC3895 phase-shift modulator. Four gate drive signals are

generated by UCC3895 based on the control signal (which determines the required phase difference between the transformer’s primary and secondary voltages). “Out A1” and “Out B1” are used to drive the primary half-bridge’s MOSFETs, and “Out C1” and “Out D1” are used to drive the secondary half-bridge’s MOSFETs. The battery branch is controlled by a PI+PR controller already discussed in Section 4. Similar to the fuel cell branch, the PI+PR controller produces a control signal for another UCC3895 phase-shift modulator that generates the gate drive signals for driving the primary half-bridge’s MOSFETs of the battery branch. Since the two primary half-bridge cells share a common secondary half-bridge cell, the transformer’s secondary voltage is used as the reference for phase-shift control, thus the two UCC3895 phase-shift modulators are synchronized by applying a common synchronization signal to the “Sync” pin.

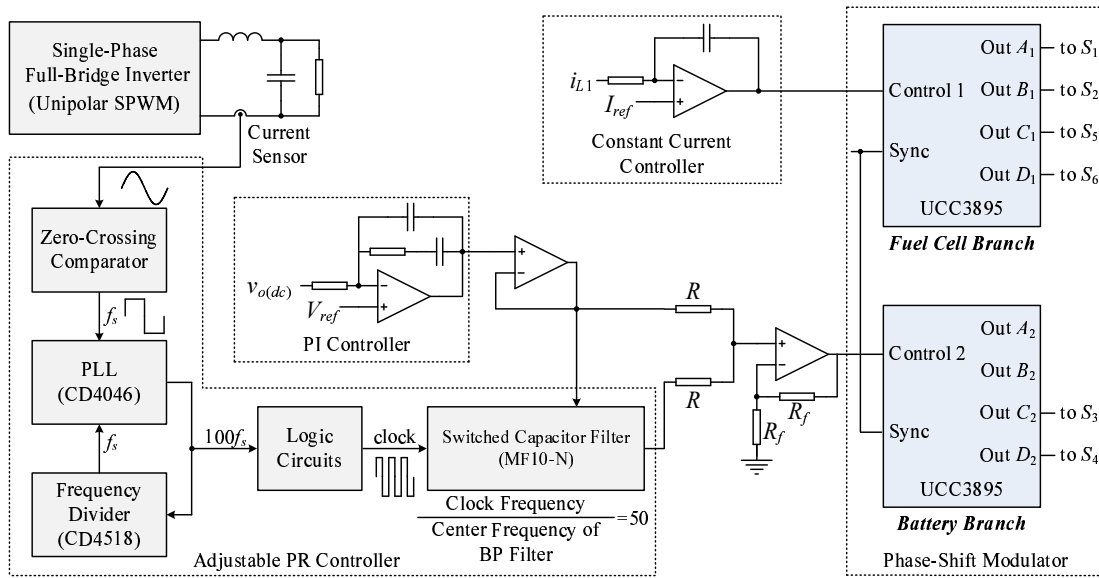


Figure 14: Overall control block diagram of the two-input bi-directional DAB dc-dc converter.

Fig. 15 shows the steady-state waveforms of the transformer’s primary voltage, secondary voltage, and leakage inductor current for four possible scenarios, *i.e.* when (a) fuel cell delivers power, (b) battery delivers power, (c) battery absorbs power, and (d) battery at rest. It can be seen that these waveforms correlate closely with the theoretical waveforms depicted in Fig. 5.

In order to verify the effectiveness of the proposed frequency-adaptive PR controller, the main converter waveforms were captured for three inverter frequencies and shown in Fig. 16 (40 Hz), Fig. 17 (50 Hz), and Fig. 18 (60 Hz). For each of these figures, (a) and (b) shows the waveforms of the converter employing PI control and PI+PR control, respectively. Four traces are shown in each of these figures, where i_{fc} is the fuel cell’s output current, i_{bat} is the battery’s output current, $v_{o(dc)}$ is the output dc bus voltage, and $v_{o(inv)}$ is the

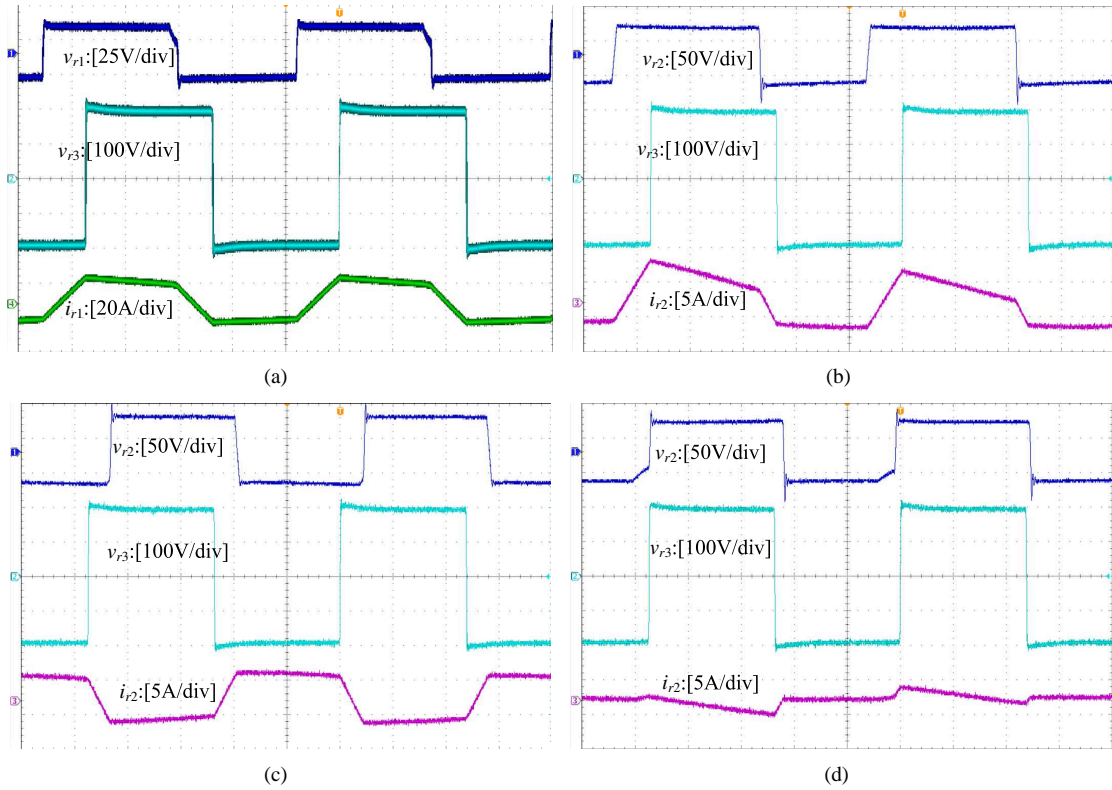
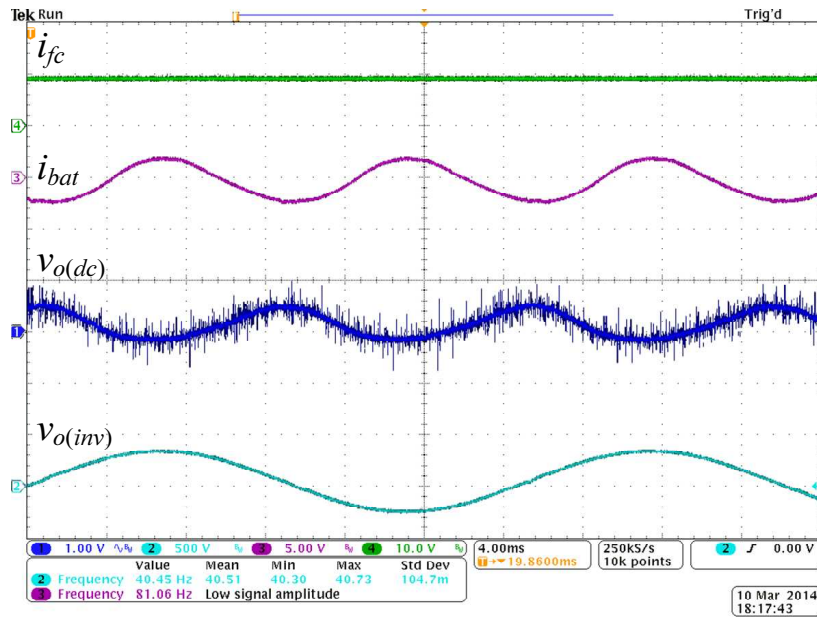


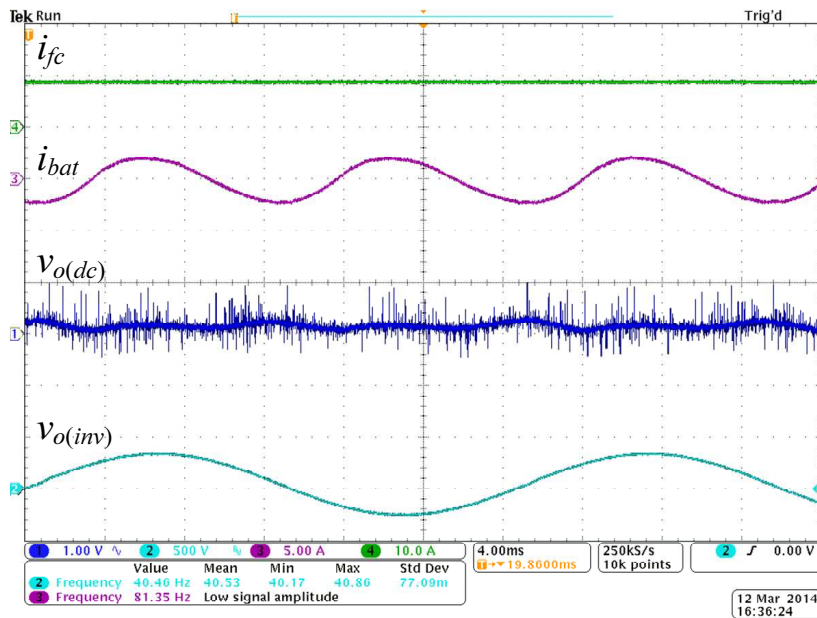
Figure 15: Steady-state transformer's primary voltage, secondary voltage, and leakage inductor current waveforms for the case when (a) fuel cell delivers power, (b) battery delivers power, (c) battery absorbs power, and (d) battery at rest.

inverter's output voltage. For the dc bus voltage, only the ac-coupled waveform is shown in order to give a magnified and clear view of the ac ripple voltage. In all cases, it can be seen that no harmonic current is drawn from the fuel cell branch due to the high output impedance that it presents to the harmonic current flow, as intended by design, and the harmonic current is mainly delivered by the battery branch. However, for the converter employing PI control only, a portion of the harmonic current is also drawn from the output dc-link capacitor, thus causing the presence of a significant harmonic voltage component at $2f_s$ in the output dc bus voltage. By including PR control, it can be seen that the size of this harmonic voltage component is considerably attenuated. Similar harmonic voltage reduction performances are observed for all three inverter frequencies, indicating that the frequency-adaptive PR controller is capable of tracking the inverter frequency accurately and maintaining effective harmonic current absorption by the battery branch.

In order to quantify the harmonic-voltage-reduction performance of the proposed frequency-adaptive PI+PR control more accurately, FFT analyses were performed on the dc bus voltage waveform. The spectra of the dc bus voltage with PI control and PI+PR control are shown in Fig. 19, Fig. 20, and Fig. 21 for $f_s = 40, 50,$ and



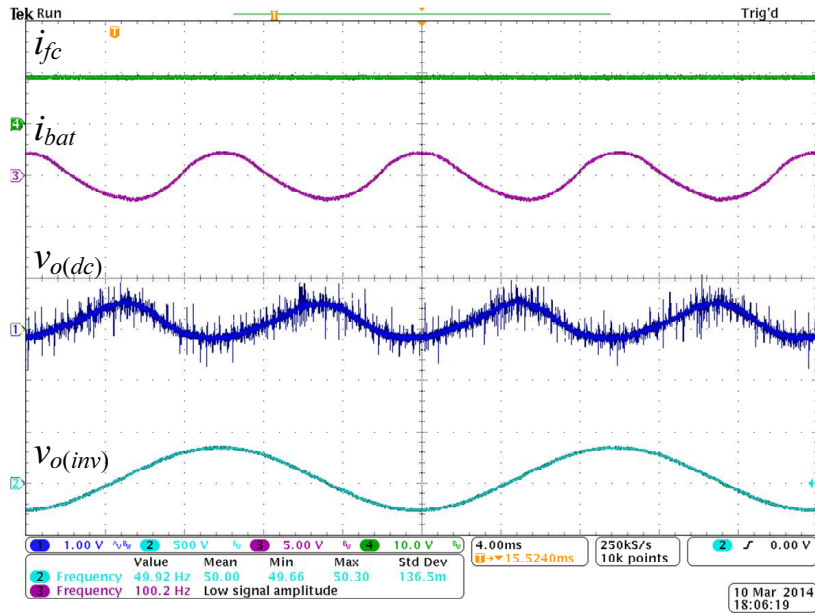
(a)



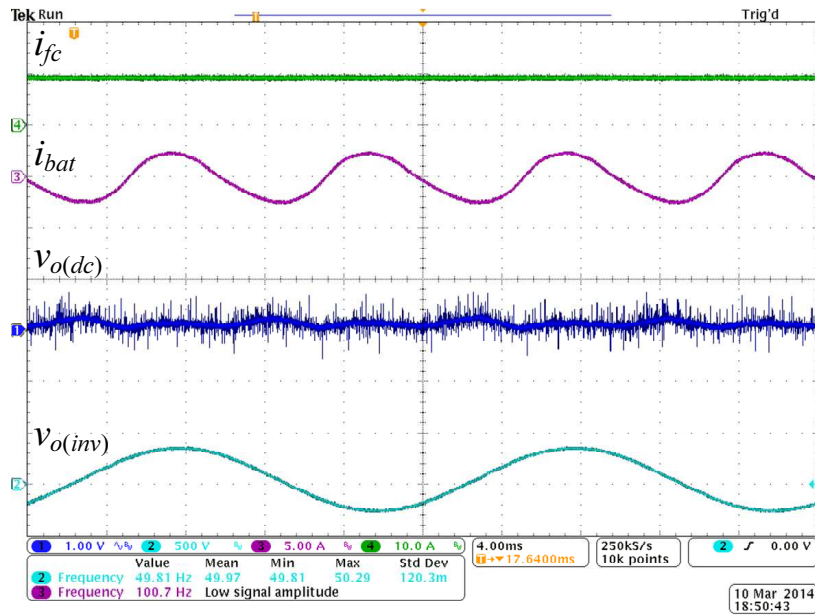
(b)

Figure 16: Static converter waveforms at $f_s = 40$ Hz with (a) PI control only; and (b) PI+PR control (Labels: i_{fc} is the fuel cell's output current, i_{bat} is the battery's output current, $v_o(dc)$ is the dc bus voltage (ac-coupled), and $v_o(inv)$ is the inverter's output voltage).

60 Hz, respectively. By comparing the magnitudes of the $2f_s$ -component with PI control and PI+PR control, it can be calculated that the harmonic voltage component is attenuated by 86.6%, 90.4%, and 87.7% for $f_s =$



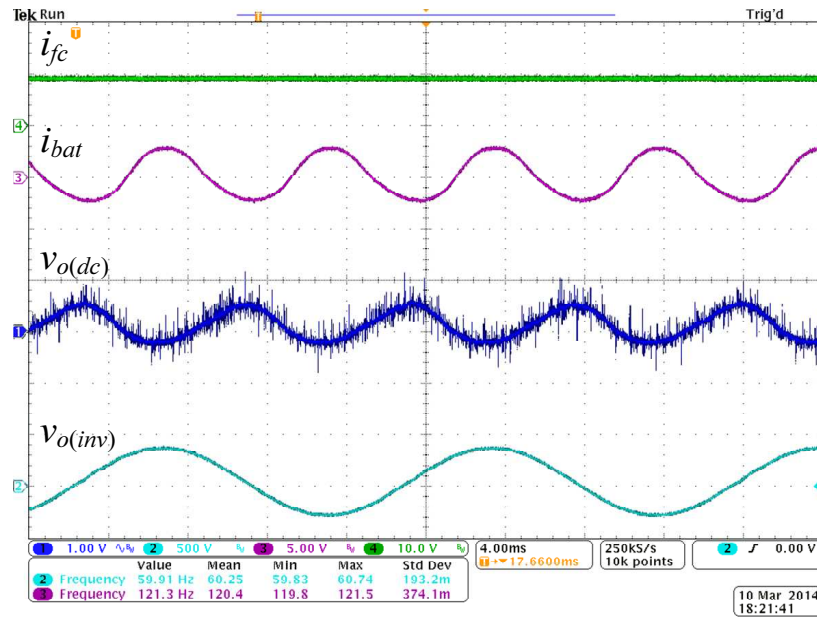
(a)



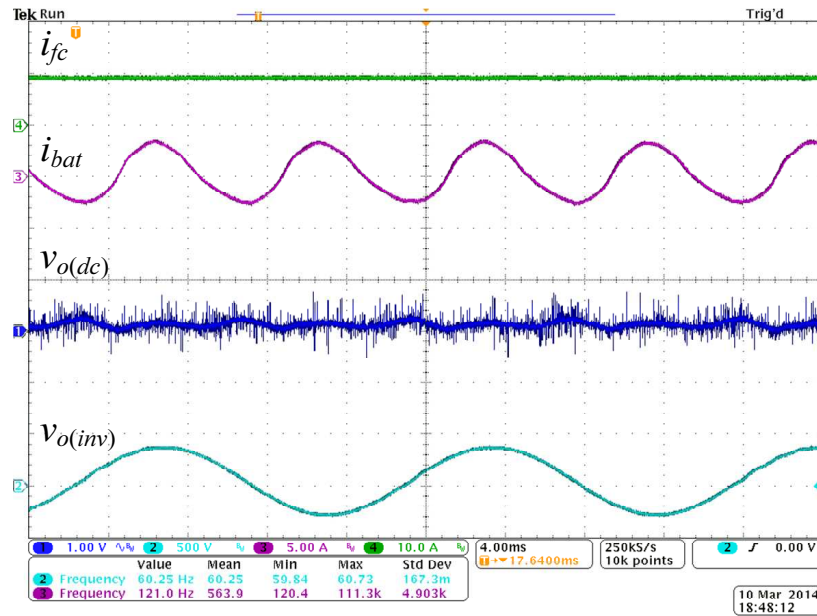
(b)

Figure 17: Static converter waveforms at $f_s = 50$ Hz with (a) PI control only; and (b) PI+PR control (Labels: i_{fc} is the fuel cell's output current, i_{bat} is the battery's output current, $v_{o(dc)}$ is the dc bus voltage (ac-coupled), and $v_{o(inv)}$ is the inverter's output voltage).

40, 50, and 60 Hz, respectively. The similarly high percentage attenuation experienced by the harmonic voltage component for all three grid frequencies can be attributed to the frequency-adaptiveness of the proposed PI+PR



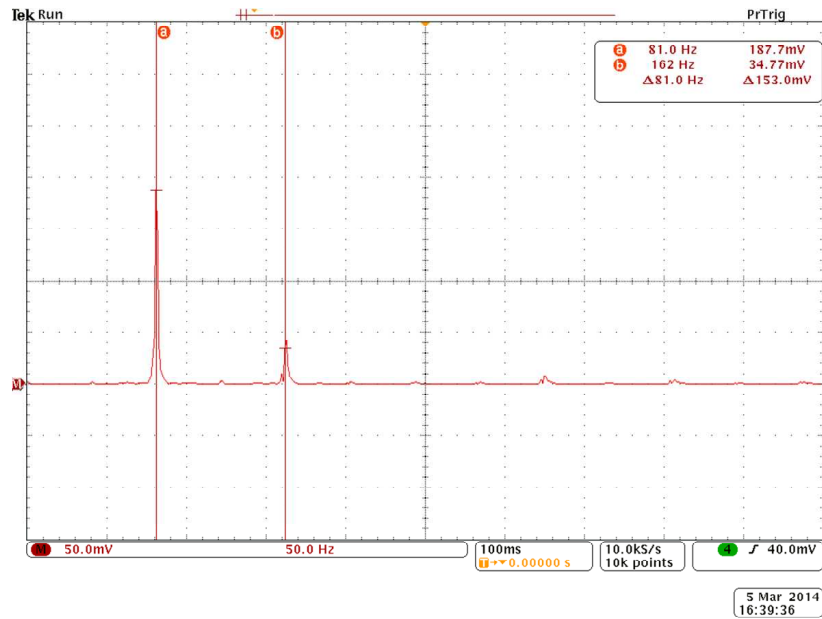
(a)



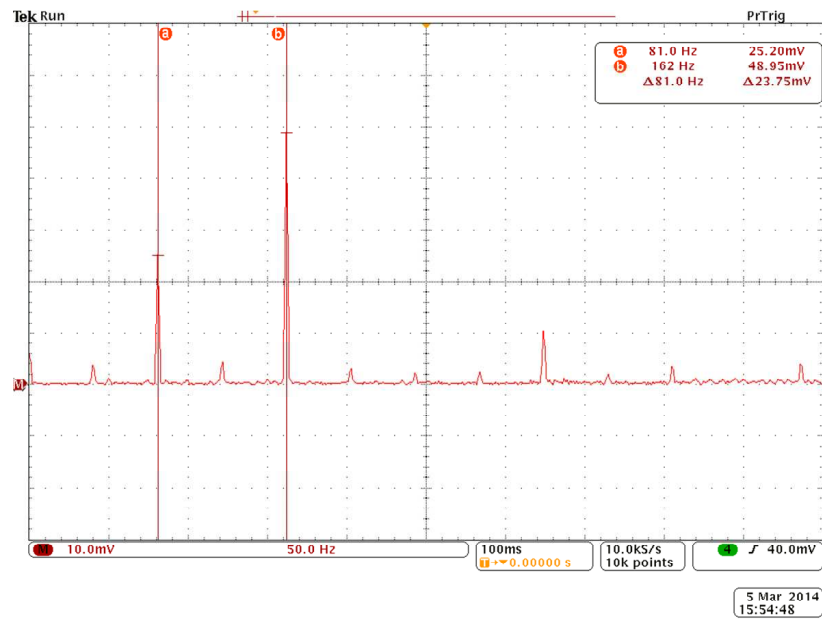
(b)

Figure 18: Static converter waveforms at $f_s = 60$ Hz with (a) PI control only; and (b) PI+PR control (Labels: i_{fc} is the fuel cell's output current, i_{bat} is the battery's output current, $v_{o(dc)}$ is the dc bus voltage (ac-coupled), and $v_{o(inv)}$ is the inverter's output voltage).

controller, which consistently tracks the grid frequency and provides the high loop gain required for tightly regulating the dc bus voltage.



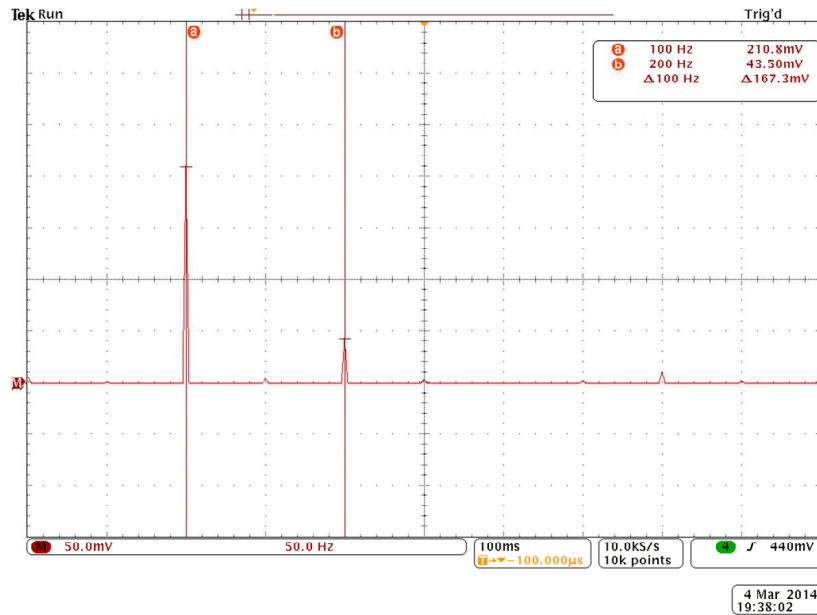
(a)



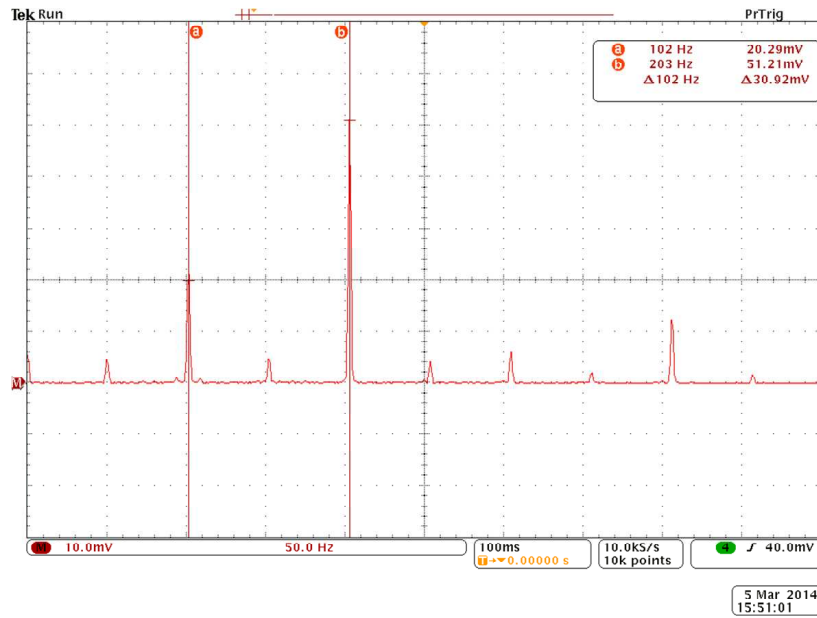
(b)

Figure 19: FFT analysis of the dc bus voltage at $f_s = 40$ Hz with (a) PI control only; and (b) PI+PR control.

Next, the dynamic response of the prototype converter was tested by introducing a load change in the inverter, with the inverter's load stepped from half-load to full-load. Comparisons were made between the PI and PI+PR control schemes under three grid frequencies (40, 50, and 60 Hz), and the measured waveforms are shown in Fig. 22 to Fig. 24. In general, the converter shows similar behavior under all three grid frequencies.



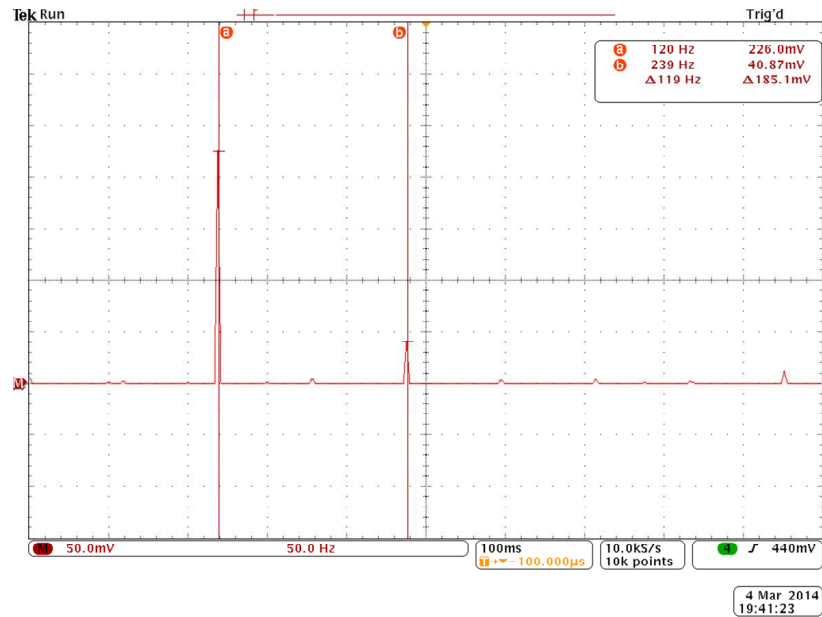
(a)



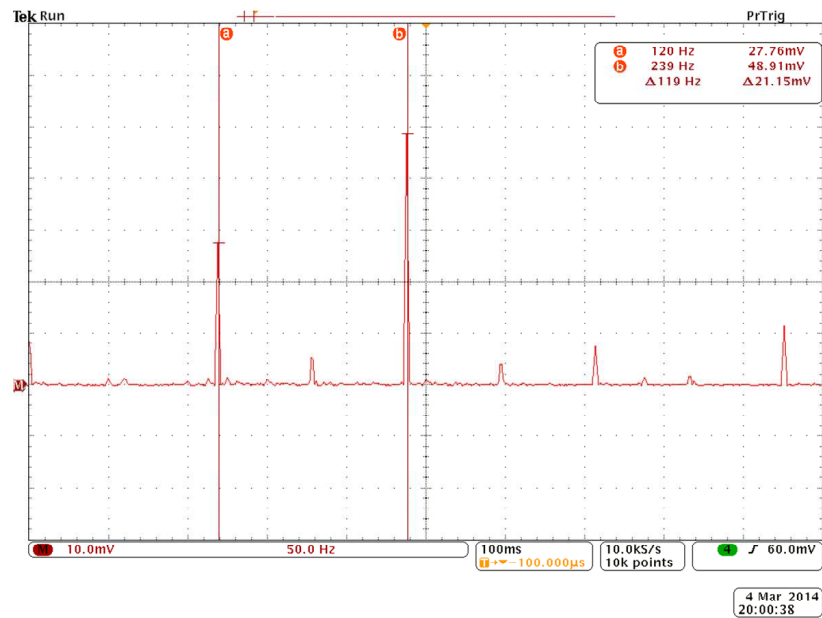
(b)

Figure 20: FFT analysis of the dc bus voltage at $f_s = 50$ Hz with (a) PI control only; and (b) PI+PR control.

Since the fuel cell is controlled to deliver a constant power, the difference between the fuel cell's output power and the load power flows into the battery and provides charging power to it, as can be verified by the negative battery's output current. As the inverter's load is stepped to full-load, the fuel cell's output power is equal to the average power consumed by the inverter, while the fluctuating instantaneous power at $2f_s$ is absorbed by the



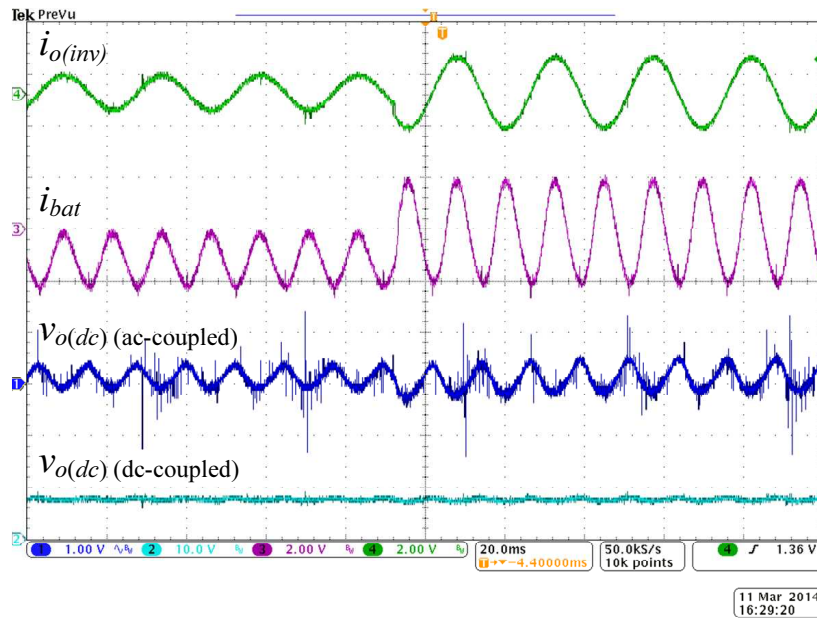
(a)



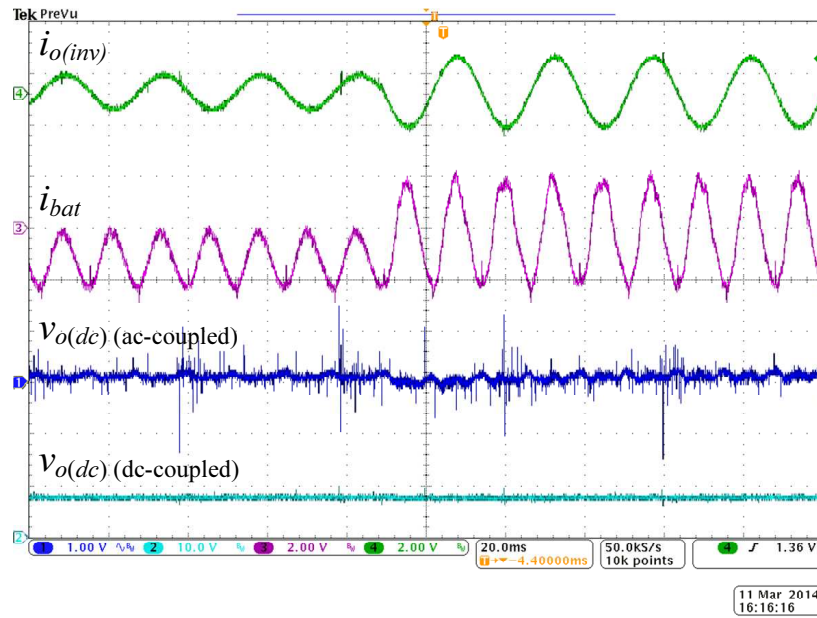
(b)

Figure 21: FFT analysis of the dc bus voltage at $f_s = 60$ Hz with (a) PI control only; and (b) PI+PR control.

battery. Thus, the average battery's output current is zero. Comparing the case with PI control to the one with PI+PR control, it is observed that the amplitude of the battery's output current is increased when PI+PR control is employed due to the increased loop gain at the harmonic frequency of interest ($2f_s$), hence less harmonic current is drawn from the dc-link capacitor, resulting in a significant reduction in the amplitude of the harmonic



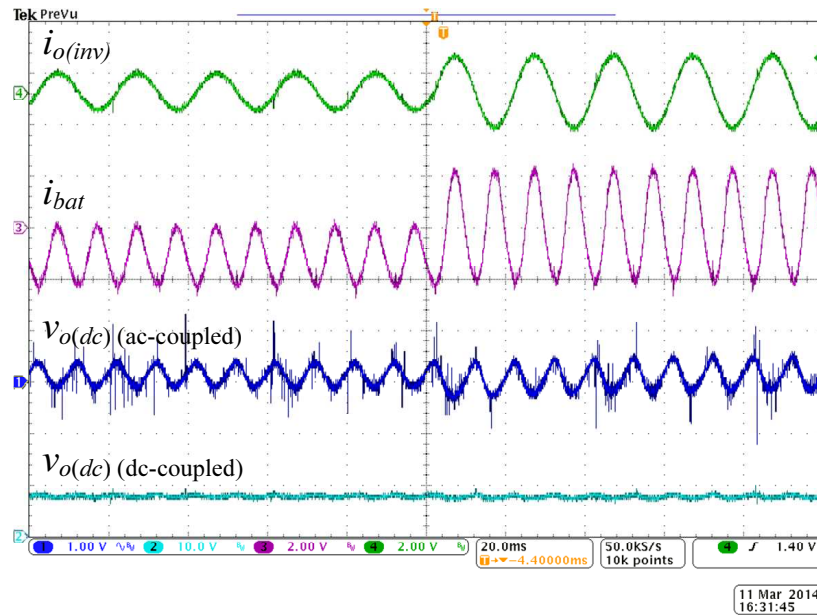
(a)



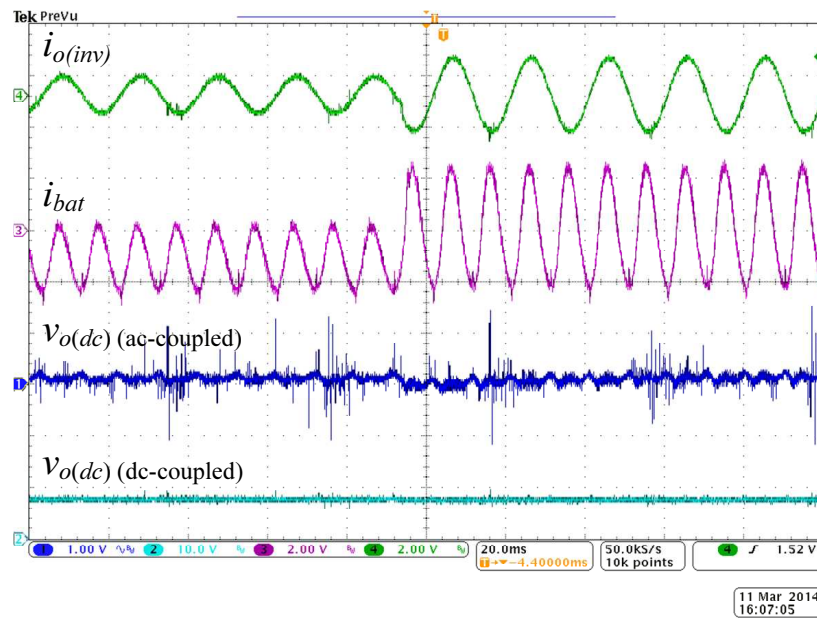
(b)

Figure 22: Dynamic converter waveforms at $f_s = 40$ Hz with (a) PI control only; and (b) PI+PR control (Labels: $i_{o(inv)}$ is the inverter's output current, i_{bat} is the battery's output current, $v_{o(dc)(ac-coupled)}$ is the ac-coupled dc bus voltage, and $v_{o(dc)(dc-coupled)}$ is the dc-coupled dc bus voltage (with 390-V dc offset)).

voltage component on the dc bus voltage. The absence of noticeable voltage undershoot on the dc bus voltage waveform verifies that the adoption of PI+PR control, when properly designed, does not degrade the stability



(a)

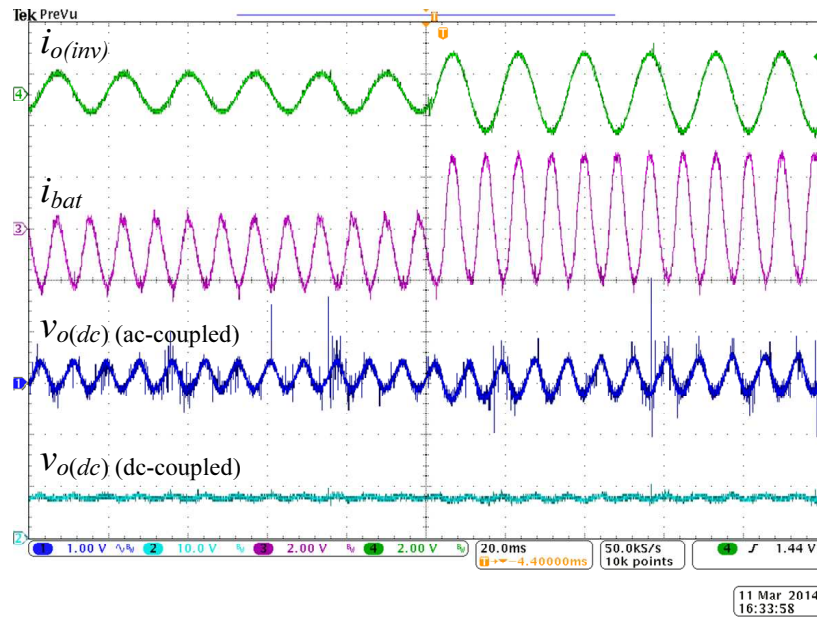


(b)

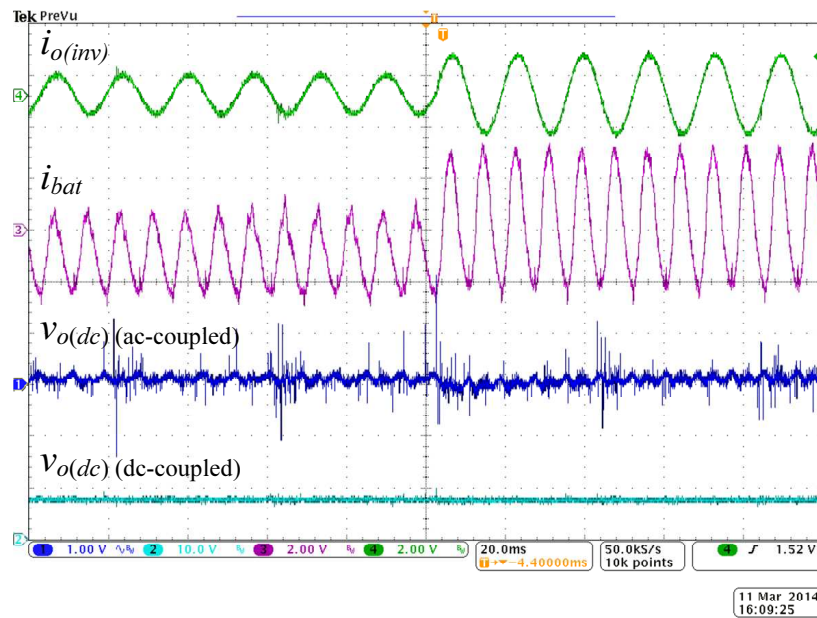
Figure 23: Dynamic converter waveforms at $f_s = 50$ Hz with (a) PI control only; and (b) PI+PR control (Labels: $i_{o(inv)}$ is the inverter's output current, i_{bat} is the battery's output current, $v_{o(dc)(ac-coupled)}$ is the ac-coupled dc bus voltage, and $v_{o(dc)(dc-coupled)}$ is the dc-coupled dc bus voltage (with 390-V dc offset)).

and dynamic response performance of the converter.

Finally, the conversion efficiencies of the prototype converter were measured for three operating modes: (1)



(a)



(b)

Figure 24: Dynamic converter waveforms at $f_s = 60$ Hz with (a) PI control only; and (b) PI+PR control (Labels: $i_{o(inv)}$ is the inverter's output current, i_{bat} is the battery's output current, $v_{o(dc)(ac-coupled)}$ is the ac-coupled dc bus voltage, and $v_{o(dc)(dc-coupled)}$ is the dc-coupled dc bus voltage (with 390-V dc offset)).

both the fuel cell and the battery deliver power to the load (point A in Fig. 25); (b) the fuel cell delivers power to the load while the battery is at rest (point B in Fig. 25); and (3) the fuel cell delivers power to the battery,

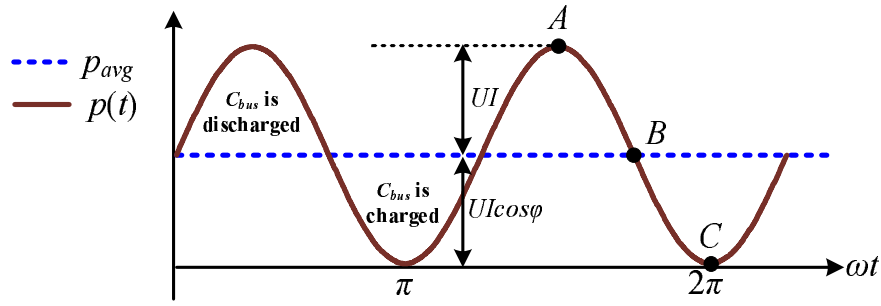


Figure 25: Three operating modes of two-input bi-directional DAB dc-dc converter.

thus charging the battery (point C in Fig. 25). For these measurements, the fuel cell's output power is kept constant at ~ 160 W, and the battery's output power is ~ 160 W when discharging or ~ -160 W when charging. The measured conversion efficiency is (1) 89.2%; (2) 87.8%; and (3) 89.2% for the corresponding operating mode. In all these measurements, conversion efficiency is defined as the ratio between the total load power and the total source power, where the battery is treated as *source* in mode (1) and *load* in mode (3).

6 Conclusion

The effectiveness of harmonic current absorption by the energy storage branch in a fuel cell power conditioning system based on two-input DAB dc-dc converter was studied. The output impedance of the energy storage branch under open-loop condition, as well as closed-loop conditions with single-voltage-loop and dual-loop controls, were analyzed and compared. It was found that, although the existing voltage-control strategies are shown to be effective in lowering the output impedance of the energy storage branch, significant voltage ripples still exist on the dc voltage bus. The introduction of PR control was experimentally shown to be very effective in suppressing these voltage ripples by diverting harmonic current flow from the dc-link capacitor to the energy storage branch. A low-cost, analogue-based frequency-adaptive PR controller was proposed to track the harmonic frequency changes and its performance over the reported range of grid frequency variation, *i.e.* 40 Hz to 60 Hz, was experimentally verified.

Acknowledgment

This work was supported by the University Grants Committee of the Hong Kong Special Administrative Region, Research Grants Council, under Earmarked Research Grants PolyU 5185/11 and PolyU 5390/13.

References

- [1] S. K. Pradhan, S. K. Mazumder, J. Hartvigsen, and M. Hollist, "Effects of Electrical Feedbacks on Planar Solid Oxide Fuel Cell," *Journal of Fuel Cell Science and Technology*, vol. 4, no. 2, pp. 154–166, May 2007
- [2] G. Fontes, C. Turpin, R. Saisset, T. Meynard, and S. Astier, "Interactions between Fuel Cells and Power Converters Influence of Current Harmonics on a Fuel Cell Stack," *IEEE Transactions on Power Electronics*, vol. 22, no. 2, pp. 670–678, March 2007
- [3] R. Ferrero, M. Marracci, and B. Tellini, "Single PEM Fuel Cell Analysis for the Evaluation of Current Ripple Effects," *IEEE Transactions on Instrumentation and Measurement*, vol. 62, no. 5, pp. 1058–1064, May 2013
- [4] W. Choi, P. N. Enjeti, J. W. Howze, and G. Joung, "An Experimental Evaluation of the Effects of Ripple Current Generated by the Power Conditioning Stage on a Proton Exchange Membrane Fuel Cell Stack," *Journal of Materials Engineering and Performance*, vol. 13, no. 3, pp. 257–264, June 2004
- [5] F. Sergi, G. Brunaccini, A. Stassi, A. Di Blasi, G. Dispenza, A. S. Arico, M. Ferraro, and V. Antonucci, "PEM Fuel Cells Analysis for Grid Connected Applications," *International Journal of Hydrogen Energy*, vol. 36, no. 17, pp. 10908–10916, August 2011
- [6] K. Fukushima, I. Norigoe, M. Shoyama, T. Ninomiya, Y. Harada, and K. Tsukakoshi, "Input Current-Ripple Consideration for the Pulse-Link DC-AC Converter for Fuel Cells by Small Series LC Circuit," *Twenty-Fourth Annual IEEE Applied Power Electronics Conference and Exposition, 2009, APEC 2009*, 15–19 February 2009, pp. 447–451
- [7] C. Liu and J. S. Lai, "Low Frequency Current Ripple Reduction Technique With Active Control in a Fuel Cell Power System With Inverter Load," *IEEE Transactions on Power Electronics*, vol. 22, no. 4, pp. 1429–1436, July 2007
- [8] R. Bojoi, C. Pica, D. Roiu, and A. Tenconi, "New DC-DC Converter with Reduced Low-Frequency Current Ripple for Fuel Cell in Single-Phase Distributed Generation," *IEEE International Conference on Industrial Technology (ICIT)*, 14–17 March 2010, pp. 1213–1218
- [9] Y. J. Song and P. N. Enjeti, "A High Frequency Link Direct DC-AC Converter for Residential Fuel Cell Power Systems," *IEEE 35th Annual Power Electronics Specialists Conference, PESC 04*, 20–25 June 2004, pp. 4755–4761

- [10] J. M. Kwon, E. H. Kim, B. H. Kwon, and K. H. Nam, "High-Efficiency Fuel Cell Power Conditioning System With Input Current Ripple Reduction," *IEEE Transactions on Industrial Electronics*, vol. 56, no. 3, pp. 826–834, March 2009
- [11] X. Liu, H. Li, and Z. Wang, "A Fuel Cell Power Conditioning System With Low-Frequency Ripple-Free Input Current Using a Control-Oriented Power Pulsation Decoupling Strategy," *IEEE Transactions on Power Electronics*, vol. 29, no. 1, pp. 159–169, January 2014
- [12] P. T. Krein, R. S. Balog, and M. Mirjafari, "Minimum Energy and Capacitance Requirements for Single-Phase Inverters and Rectifiers Using a Ripple Port," *IEEE Transactions on Power Electronics*, vol. 27, no. 11, pp. 4690–4698, November 2012
- [13] C. Y. Hsu, and H. Y. Wu, "A New Single-Phase Active Power Filter with Reduced Energy-Storage Capacity," *IEE Proceedings–Electric Power Applications*, vol. 143, no. 1, pp. 25–30, January 1996
- [14] A. C. Kyritsis, N. P. Papanikolaou, and E. C. Tatakis, "A Novel Parallel Active Filter for Current Pulsation Smoothing on Single Stage Grid-connected AC-PV Modules," *European Conference on Power Electronics and Applications*, 2–5 September 2007, pp. 1–10
- [15] J. L. Duarte, M. Hendrix, and M. G. Simoes, "Three-port Bi-directional Converter for Hybrid Fuel Cell Systems," *IEEE Transactions on Power Electronics*, vol. 22, no. 2, pp. 480–487, March 2007
- [16] H. Tao, A. Kotsopoulos, J. L. Duarte, and M. A. M. Hendrix, "Transformer-coupled Multiport ZVS Bi-directional DC-DC Converter with Wide Input Range," *IEEE Transactions on Power Electronics*, vol. 23, no. 2, pp. 771–781, March 2008
- [17] D. Liu and H. Li, "A ZVS Bi-directional DC-DC Converter for Multiple Energy Storage Elements," *IEEE Transactions on Power Electronics*, vol. 21, no. 5, pp. 1513–1517, September 2006
- [18] X. Li, W. Zhang, H. Li, R. Xie, M. Chen, G. Shen, and D. Xu, "Power Management Unit With Its Control for a Three-Phase Fuel Cell Power System Without Large Electrolytic Capacitors," *IEEE Transactions on Power Electronics*, vol. 26, no. 12, pp. 3766–3777, July 2011
- [19] F. D. Freijedo, A. G. Yepes, J. Malvar, O. Lopez, P. Fernandez-Comesana, A. Vidal, and J. Doval-Gandoy, "Frequency Tracking of Digital Resonant Filters for Control of Power Converters Connected to Public Distribution Systems," *IET Power Electronics*, vol. 4, no. 4, pp. 454–462, 2011

- [20] J. M. Guerrero, J. C. Vasquez, J. Matas, L. Garcia de Vicuna, and M. Castilla, "Hierarchical Control of Droop-Controlled AC and DC Microgrids—A General Approach Toward Standardization," *IEEE Transactions on Power Electronics*, vol. 58, no. 1, pp. 158–172, January 2011
- [21] H. Li, F. Z. Peng, and J. S. Lawler, "A Natural ZVS Medium-power Bidirectional DC-DC Converter with Minimum Number of Devices," *IEEE Transactions on Industry Applications*, vol. 39, no. 2, pp. 525–535, March 2003
- [22] D. N. Zmood and D. G. Holmes, "Stationary Frame Current Regulation of PWM Inverters with Zero Steady-State Error," *IEEE Transactions on Power Electronics*, vol. 18, no. 3, pp. 814–822, May 2003
- [23] H. Qin and J. W. Kimball, "Closed-Loop Control of DC-DC Dual-Active-Bridge Converters Driving Single-Phase Inverters," *IEEE Transactions on Power Electronics*, vol. 29, no. 2, pp. 1006–1017, February 2014
- [24] Z. Wei, X. Deng, C. Gong, J. Chen, and F. Zhang, "A Novel Technique of Low Frequency Input Current Ripple Reduction in Two-Stage DC-AC Inverter," *The 38th Annual Conference on IEEE Industrial Electronics Society, 2012, IECON 2012*, 25–28 October 2012, pp. 139–143